JACS
JOURNAL OF THE AMERICAN CHEMICAL SOCIETY
Article
pubs.acs.org/JACS

Preparation, Structure, and Electrochemistry of Layered Polyanionic Hydroxysulfates: $LiMSO_4OH$ (M = Fe, Co, Mn) Electrodes for Li-Ion Batteries

Chinmayee V. Subban,[†,∥] Mohamed Ati,[†,‡,∥] Gwenaëlle Rousse,[§] Artem M. Abakumov,[⊥] Gustaaf Van Tendeloo,[⊥] Raphaël Janot,[†] and Jean-Marie Tarascon*[,†,‡,∥]

[†]Laboratoire de Réactivité et Chimie des Solides, UMR CNRS 7314, Université de Picardie Jules Verne, 33 rue Saint-Leu, 80039 Amiens Cedex, France

[‡]ALISTORE—European Research Institute, 80039 Amiens Cedex, France

[§]Institut de Minéralogie et de Physique des Milieux Condensés, UMR CNRS 7590, Université Pierre et Marie Curie, 4 Place Jussieu, 75252 Paris Cedex 05, France

[⊥]EMAT, University of Antwerp, Groenenborgerlaan 171, B-2020 Antwerp, Belgium

[∥]Réseau sur le Stockage Electrochimique de l'Energie (RS2E), CNRS FR3459, 80039 Amiens Cedex, France

Supporting Information

ABSTRACT: The Li-ion rechargeable battery, due to its high energy density, has driven remarkable advances in portable electronics. Moving toward more sustainable electrodes could make this technology even more attractive to large-volume applications. We present here a new family of 3d-metal hydroxysulfates of general formula $LiMSO_4OH$ (M = Fe, Co, and Mn) among which (i) $LiFeSO_4OH$ reversibly releases 0.7 Li^+ at an average potential of 3.6 V vs Li^+/Li^0, slightly higher than the potential of currently lauded $LiFePO_4$ (3.45 V) electrode material, and (ii) $LiCoSO_4OH$ shows a redox activity at 4.7 V vs Li^+/Li^0. Besides, these compounds can be easily made at temperatures near 200 °C via a synthesis process that enlists a new intermediate phase of composition $M_3(SO_4)_2(OH)_2$ (M = Fe, Co, Mn, and Ni), related to the mineral *caminite*. Structurally, we found that $LiFeSO_4OH$ is a layered phase unlike the previously reported 3.2 V *tavorite* $LiFeSO_4OH$. This work should provide an impetus to experimentalists for designing better electrolytes to fully tap the capacity of high-voltage Co-based hydroxysulfates, and to theorists for providing a means to predict the electrochemical redox activity of two polymorphs.

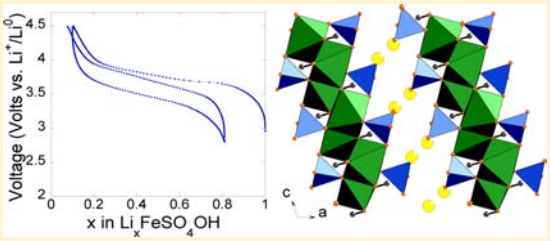

INTRODUCTION

Li-ion batteries have conquered the world of portable electronics and are among the leading technologies being considered to power electric vehicles. They are also considered a serious candidate within the field of renewable sources (wind and solar) for balancing intermittency with user demands. However, for this technology to support such large-volume markets, efforts must be focused on increasing their energy density and lowering their costs, while simultaneously addressing sustainability issues.

Significant research has been devoted to substituted layered oxides, which have shown capacities as high as 250 mAh/g for an average voltage of 3.8 V vs Li^+/Li.[1] While these layered oxides have satisfactory energy densities, their cost due to the transition metals (Co and Ni) and the high cost of synthesis of active phases make them less feasible for large-volume applications. Alternatively, efforts are being directed toward the development of Fe-based polyanionic compounds such as $LiFePO_4$,[2] Li_2FeSiO_4,[3] $Li_2FeP_2O_7$,[4] and $LiFeBO_3$.[5] These Fe-based compounds present low-cost advantages due to both the abundance of their constituent elements and the feasibility, in most cases, of using efficient synthesis methods to prepare them. However, these Fe-based materials present much lower energy densities compared to the layered oxide materials. Hence, combining the electronegativity of fluorine and the inductive effect[6] enhanced by the presence of a SO_4^{2-} polyanion in the structure, our group recently developed a new family of fluorosulfates of the general formula A_xMSO_4F, where A = Li, Na, K and M = 3d metals.[7−15] Among them, $LiFeSO_4F$ turns out to be the most interesting from the point of view of both crystal chemistry and electrochemical performance. $LiFeSO_4F$ exists as two polymorphs, *tavorite* and *triplite*, whose redox potentials are 3.6 and 3.9 V vs Li^+/Li^0, respectively.[7,13,15] With the highest ever reported Fe^{3+}/Fe^{2+} redox voltage for any inorganic compound, *triplite* $LiFeSO_4F$ presents a theoretical energy density (577 Wh/kg) which is comparable to that of $LiFePO_4$. Besides, we recently showed that this phase can be made at room temperature via mechanochemical synthesis, which suggests easy scalability

Received: December 23, 2012
Published: February 1, 2013

   dx.doi.org/10.1021/ja3125492 | J. Am. Chem. Soc. 2013, 135, 3653−3661

and low-cost synthesis.[11] However, it may be argued that such fluorosulfate materials are not ideal electrodes as they contain fluorine, although it must be noted that today's commercial cells use both F-based binders and electrolytes. Nonetheless, we decided to investigate the possibility of preparing fluorine-free 3d-metal sulfate electrode materials.

An obvious choice, based on the existence of numerous minerals with either F^- or OH^- anions, was to move to hydroxysulfates, but they have been previously explored. In fact, Pralong et al. have reported *tavorite* $FeSO_4OH$, into which Li can be inserted at 3.2 V vs Li^+/Li^0, a voltage penalty of 400 mV compared to *tavorite* $LiFeSO_4F$.[10,16] The *tavorite* $LiFeSO_4OH$ was prepared by electrochemical insertion of Li into $FeSO_4OH$, and to our knowledge, the direct synthesis of $LiFeSO_4OH$ has not been reported. Based on the polymorphism observed in $LiFeSO_4F$, we decided to explore whether a similar phenomenon existed in $LiFeSO_4OH$. We started by simply implementing our mechanochemical synthesis approach (via ball-milling), which was previously used to prepare *triplite* $LiFeSO_4F$,[11] to the synthesis of 3d-metal hydroxysulfates $LiMSO_4OH$ (M = Fe, Co, Mn, and Ni). With the exception of Ni, this approach in combination with a nominal heat treatment turns out to be successful, as we herein report the synthesis of a new family of $LiMSO_4OH$ phases (M = Fe, Co, and Mn) which crystallize in a layered structure different from any of the known polymorphs for the fluorine-based analogues. Of this family of materials, Fe and Co phases present high-voltage redox activity toward Li^+/Li^0 of 3.6 and 4.7 V, respectively. In this paper we report the synthesis of these phases together with the determination of their crystal structure and their electrochemical properties. Additionally, through the mechanochemical synthesis of these 3d-metal hydroxysulfates, we could isolate an intermediate Li-free $M_3(SO_4)_2(OH)_2$ (M = Fe, Co, Mn, and Ni) phase which adopts the mineral *caminite* $Mg_3(SO_4)_2(OH)_2$ structure.

EXPERIMENTAL METHODS

Ball-Milling Apparatus. Ball-milling was conducted using either a Spex 8000 or a Retsch PM100 miller, and the hard steel ball-mill jars were filled and emptied in an Ar-filled glovebox. The ball-to-powder weight ratio was maintained between 30 and 50.

X-ray and Neutron Powder Diffraction. Powder X-ray diffraction (PXRD) measurements were conducted using a Bruker D8 diffractometer with a Co Kα radiation source (λ_1 = 1.78897 Å, λ_2 = 1.79285 Å) and a Vantec detector. Neutron powder diffraction (NPD) was performed on some of the pristine samples (M = Mn and Fe) on the D2B high-resolution powder diffractometer (Institut Laue Langevin, Grenoble, France) with a wavelength of λ = 1.5942 Å. Rietveld refinements[17] of the resulting patterns were conducted using the FullProf program.[18]

The *in situ* XRD measurements were conducted in a stainless steel cell with an X-ray-transparent beryllium window. The window was protected from high-voltage-related oxidation by a thin layer of aluminum, which also functioned as a current collector. The *in situ* XRD patterns were collected for a complete charge/discharge cycle versus lithium metal as the negative electrode.

Microscopy Studies. The $LiFeSO_4OH$ samples were prepared for transmission electron microscopy (TEM) studies in an Ar glovebox and transported to the microscope under Ar. The powder sample was ground using a mortar and pestle prior to dispersing in anhydrous ethanol, and then a few drops of this suspension were deposited on a holey carbon grid. TEM images, electron diffraction (ED) patterns, and energy dispersive X-ray (EDX) spectra were obtained with a Tecnai G^2 electron microscope operated at 200 kV.

Thermogravimetric Analysis (TGA). The thermal stability of $LiMSO_4OH$ samples was studied by heating them in an alumina crucible under Ar flow at 10 K/min to 700 °C, on a Netzsch STA 449C apparatus.

Electrochemical Testing. The working electrode was prepared by mixing the active electrode material with 25 wt% SP carbon using a ball-mill for 20 min. The material was then tested in Swagelok-type cells, with Li metal as negative electrode, Whatman GF/D borosilicate glass fiber separator, and an LP100 electrolyte (1 M $LiPF_6$ solution in a 1:1:3 weight mixture of ethylene carbonate, propylene carbonate, and dimethyl carbonate). The cells were assembled in an Ar environment and generally contained 6−10 mg of active material per cell. Galvanostatic charge/discharge tests were conducted at 20 °C using a "Mac-Pile" or a VMP system (Biologic S.A., Claix, France).

RESULTS

1. Synthesis and X-ray Characterization. Ball-milling has been extensively used in Li batteries to (i) shape material size and morphology, (ii) stabilize new Li-based intermetallic phases, or (iii) combine the active electrode material with carbon.[19,20] Our previous experience and success with synthesis of $LiFeSO_4F$ via ball-milling[11] inspired the exploration of the technique for synthesis of $LiMSO_4OH$ materials. We experimented with two different types of ball-millers: Spex 8000, which generates normal forces (shock), and Retsch PM100, which generates mainly tangential forces (friction). Irrespective of the ball-milling apparatus, the general goal of ball-milling is to use mechanical forces to break down the particles. In addition to reducing the grain size, ball-milling induces microstructural defects. The combination of reduced diffusion distances and the induced defects is believed to aid in achieving low-temperature chemical reactions.

We attempted to prepare $LiMSO_4OH$ (M = Fe, Co, Mn, and Ni) powders via mechanical milling from mixtures of anhydrous LiOH (Alfa Aesar 99.995%) and MSO_4 precursors. The MSO_4 powders were prepared from their respective hydrated commercial precursors ($MSO_4{\cdot}nH_2O$), and the specific synthesis procedures used to obtain each of the anhydrous metal sulfates are given in Table S1. In general, the structural water was removed by heating under either Ar flow or dynamic vacuum. This step is critical, as the anhydrous nature of the 3d-metal sulfate precursors was observed to clearly affect the nature and purity of the final product. Typical experiments were conducted in an Ar drybox by weighing 1:1.15 molar ratio of MSO_4 to LiOH powders (for 1.5 g of $LiMSO_4OH$) into a ball-mill jar along with seven stainless-steel balls (7 g each). The slight excess of LiOH (1.15 mol) was used to compensate for the trace amounts of H_2O in the LiOH precursor (determined by TGA). The closed jar was then attached to either a SPEX or Retsch miller. A survey of various ball-milling parameters (weight ratio of ball to powder, ball-milling time, and cooling intervals) was explored, and a weight ratio of balls to powder between 30 and 50 was generally used.

We observed the ball-milling interval to significantly affect the nature of the final products (Figure S1). Interestingly, in Mn-, Fe-, Co-, and Ni-based samples, when the contents of the ball-milling jar were examined after 60−90 min of milling, a mixture of Li_2SO_4 and a new phase was observed. This new intermediate phase presents diffraction peaks whose 2θ position and relative intensities are similar to those of the mineral *caminite* $Mg_3(SO_4)_2(OH)_2$ [also written as $2(MgSO_4){\cdot}Mg(OH)_2$].[21] In the literature, *caminite* has been described using two tetragonal structural models: one with space group $I4_1/amd$, where Mg atoms occupy a single crystallographic site with partial 3/4 occupancy,[21] and the other with an ordering of Mg/vacancies which results in a unit cell twice as

dx.doi.org/10.1021/ja3125492 | J. Am. Chem. Soc. 2013, 135, 3653−3661

big and described by space group $P4_32_12$.[22] Rietveld refinements starting from these structural models and replacing Mg with Fe, Co, Mn, or Ni could account for all of the observed Bragg peaks. Since we do not observe superstructure peaks from ordering of metal/vacancies, we used the average $I4_1/amd$ description. Figure 1a shows the Rietveld refinement of the mixture of $Co_3(SO_4)_2(OH)_2$ and Li_2SO_4 (marked by *) against laboratory XRD pattern. The lattice parameters for M = Fe, Co, Mn, and Ni and atomic positions for M = Co are gathered in Tables 1 and 2, respectively. The unit cell volume varies nicely with the ionic radius of the transition metal.[23] A bond valence sum (BVS) analysis was performed using d_0 parameters from Brown[24] and confirmed the 2+ valence for Co. Note that we could obtain pure $Fe_3(SO_4)_2(OH)_2$ by removing Li_2SO_4 via reaction with NO_2BF_4 in acetonitrile, as shown in Figure 1a. However, a similar attempt failed to give Li_2SO_4-free Mn-, Co-, and Ni-based phases but instead resulted in decomposition of the phase. The asymmetry and peak broadening in the XRD patterns are due to disorder arising from the ball-milling process, but the peak positions and intensities clearly confirm the structural model, as shown in Figure 1. Rietveld refinement for $Mn_3(SO_4)_2(OH)_2$ is shown in Figure S2.

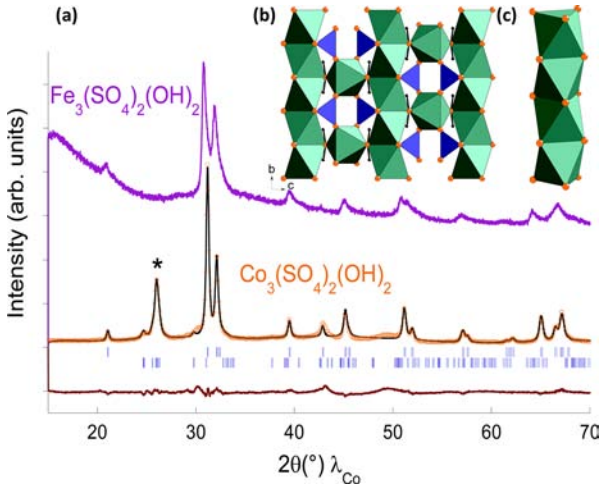

Figure 1. (a) Rietveld refinement of $Co_3(SO_4)_2(OH)_2$ XRD pattern ($\lambda_{Co}(K\alpha_1)$ = 1.78897 Å, $\lambda_{Co}(K\alpha_2)$ = 1.79285 Å). Orange, black, and brown lines correspond to the observed, calculated, and difference, respectively (R_{Bragg} = 9.2%, χ^2 = 10.4). The vertical blue tick marks correspond to the Bragg peaks of $Co_3(SO_4)_2(OH)_2$ (1st line) and Li_2SO_4 (2nd line). Li_2SO_4 is present in the sample (marked *) since $Co_3(SO_4)_2(OH)_2$ is an intermediate in the synthesis of $LiCoSO_4OH$. The pattern of $Fe_3(SO_4)_2(OH)_2$, free of Li_2SO_4, is shown in violet. (b) Structure of *caminite*-like $M_3(SO_4)_2(OH)_2$ viewed down the [100] direction. (c) A closer look at the connectivity of face-sharing MO_6 octahedra which form perpendicular chains linked through O and SO_4 tetrahedral groups. M is in the middle of 3/4 of green octahedra, SO_4 is blue, O is orange, and H occupies statistically 1/4 of the black balls.

Table 2. Structural Parameters of $Co_3(SO_4)_2(OH)_2$[a]

	Atomic Positions for $Co_3(SO_4)_2(OH)_2$					
atom	site	*x*	*y*	*z*	occupancy	BVS
Co	8*d*	0	0	1/2	3/4	1.95(1)
S	4*a*	0	3/4	1/8	1	6.52(3)
O1	16*h*	0	0.523(1)	0.187(1)	1	2.22(2)
O2	4*b*	0	1/4	3/8	1	1.56(1)
H	16*h*	0	0.47[b]	0.39[b]	1/4	0.99(1)

[a]The atomic positions are deduced from the Rietveld refinement of PXRD data. Lattice parameters and space group are reported in Table 1. The position of hydrogen atoms are not refined but assigned on the basis of the site they occupy in $Mg_3(SO_4)_2(OH)_2$ (*caminite* mineral). The table includes bond valence sum (BVS) for each atom. [b]Not refined.

To our knowledge, it is the first time that a *caminite*-like structure is reported for non-magnesium-based compositions. The structure of $M_3(SO_4)_2(OH)_2$ (M = Fe, Co, Mn, Ni) is displayed in Figure 1b,c in the average $I4_1/amd$ description. Transition metal (M) atoms sit on the 8*d* Wyckoff site with occupancy of 3/4. M atoms are located in the middle of regular O_6 octahedra, which share faces, resulting in chains running along the [100] and [010] directions. These perpendicular face-sharing octahedral chains are connected to each other via vertices and SO_4 tetrahedra. Hydrogen atoms of the hydroxyl groups could not be localized using the PXRD data and were placed in the positions reported for hydrogen in the analogous Mg structure, i.e., on a site with 1/4 occupancy. This crystal structure presents short M−M distances, as the MO_6 octahedra are face-sharing. The fact that 1/4 of the octahedra are not occupied by the transition metal assists in stabilizing the structure. Note that in the ordered model (space group $P4_32_12$) the vacancies are distributed along the face-sharing chains on every third MO_6 octahedra, which results in face-sharing trimers. The low crystallinity of our PXRD patterns limits our ability to determine possible vacancy/M ordering, but since these materials were made via ball-milling, they likely adopt a disordered model. From an electrochemical point of view, these Li-free compounds with non-reducible divalent ions (Fe, Co, Mn, and Ni) are electrochemically inactive. However, their specific structure should demonstrate magnetic frustration, which makes them interesting materials.

Upon further ball-milling, the $Fe_3(SO_4)_2(OH)_2$ phase was found to react with Li_2SO_4 and the remaining LiOH, to form a new $LiFeSO_4OH$ phase, according to the following reaction:

$$Fe_3(SO_4)_2(OH)_2 + Li_2SO_4 + LiOH \rightarrow 3LiFeSO_4OH$$

Table 1. Lattice Parameters of $M_3(SO_4)_2(OH)_2$ for M = Fe, Co, Mn, and Ni Obtained from Rietveld Refinements of Powder X-ray Diffraction Patterns[a]

	$Mn_3(SO_4)_2(OH)_2$	$Fe_3(SO_4)_2(OH)_2$	$Co_3(SO_4)_2(OH)_2$	$Ni_3(SO_4)_2(OH)_2$
ionic radius for M^{2+} (Å)	0.83	0.78	0.745	0.69
space group	$I4_1/amd$	$I4_1/amd$	$I4_1/amd$	$I4_1/amd$
a (Å)	5.438(1)	5.287(1)	5.2968(3)	5.233(2)
c (Å)	13.269(2)	13.068(3)	12.839(1)	12.633(2)
V (Å^3)	392.4(1)	365.3(1)	360.22(4)	347.1(2)

[a]Note that unit cell volumes are in agreement with M^{2+} ionic radii in octahedral coordination.

dx.doi.org/10.1021/ja3125492 | J. Am. Chem. Soc. 2013, 135, 3653−3661

$LiFeSO_4OH$ could be obtained either by two 90 min ball-mill intervals with a 10 min cooling in-between on the Spex or by a single 2 h ball-mill interval at 600 rpm, with change in direction of rotation every 20 min on the Retsch device. The single-phase samples were analyzed by infrared spectroscopy to confirm the presence of hydroxyl groups. Mössbauer spectroscopy results suggest mostly Fe^{2+} (92%) in the $LiFeSO_4OH$ samples (Figure S3). However, it should be noted that factors such as precursor purity, length of ball-milling, and the weight ratio of balls to powder were all observed to affect the final product purity. These effects were observed in samples prepared by both milling techniques.

Interestingly, such a mechanochemical process was successful only in preparing $LiFeSO_4OH$, and even upon varying the milling parameters (milling time, powder-to-ball weight ratio, Retsch vs Spex), we were unable to prepare $LiMSO_4OH$ (M = Co, Mn, and Ni) samples. Hence we explored the ceramic process to prepare these phases as described below.

$LiMSO_4OH$ materials, where M = Fe, Co, Mn, were all successfully prepared using ceramic synthesis, a method that relies on simple solid-state diffusion accelerated by increased temperatures and higher interparticle contact. An intimate mixture of 1:1.15 molar ratio of anhydrous MSO_4 to LiOH was prepared by ball-milling for 45 min on the Spex device. The mixture was then pressed into a pellet, sealed in an evacuated silica tube, and heated for 5 days. The ball-milling jars and the silica tubes were always loaded and emptied in an Ar glovebox. The desired $LiFeSO_4OH$ and $LiCoSO_4OH$ phases were obtained by heating to 185 °C, while the $LiMnSO_4OH$ required heating to 250 °C. However, the Ni phase was not obtained even upon heating to 500 °C for several days. The X-ray patterns of the $LiMSO_4OH$ samples barely changed upon the samples being exposed to air for several weeks.

This new $LiFeSO_4OH$ structure is radically different from that of the *tavorite* $FeSO_4OH$[10,16] or even the $LiFeSO_4F$ polymorphs reported thus far (*triplite*, *tavorite*, etc).[12−15,25] The unit cell parameters (a = 9.5147(1) Å, b = 5.5087(1) Å, c = 7.3755(1) Å, and β = 109.109(6)°) were determined from PXRD peak positions using the Dicvol program,[26] and the space group was determined to be monoclinic $P2_1/c$ on the basis of the observed extinctions.

The crystal structure of $LiFeSO_4OH$ was solved from PXRD data using direct methods with the EXPO software,[27] which revealed the positions of the Fe and S atoms. The positions of the O and Li atoms were obtained from difference Fourier maps using the procedure implemented in the FullProf program. Although the exact position of the H atoms is hard to determine from the present diffraction data, one can conclude that it is most likely linked to the O1 atom in the structure based on a BVS analysis. Since these compounds are made of several poor X-ray scatterers, we performed high-resolution NPD experiments on the D2B beamline to get accurate atomic positions within the structure, in particular for light elements (H, Li, O). Well-crystallized ceramic $LiMnSO_4OH$ (Rietveld refinement shown in Figure 2a) and $LiFeSO_4OH$ samples, with the latter containing small amounts of $FeSO_4{\cdot}H_2O$ and $Li_2SO_4{\cdot}H_2O$ impurity phases (less than 5%), were used in this experiment (Figure S4). Our NPD results confirmed the structure determined by XRD, and we were able to accurately determine the O, H, and Li positions. The Mn temperature factor was refined anisotropically, and the resulting ellipsoid is elongated in-plane, which indicates some kind of disorder (Table 3). This was not observed for the iron analogue, for which the refinement of anisotropic temperature factor indicates more isotropic displacements (Table 4). Note that even though the samples were not deuterated, the hydrogen position could be easily refined despite the high background due to incoherent scattering from H. The final structural models determined from NPD for Mn and Fe are listed in Tables 3 and 4 respectively. The BVSs deduced from the atomic positions are in perfect agreement with the expected valence on each atom.

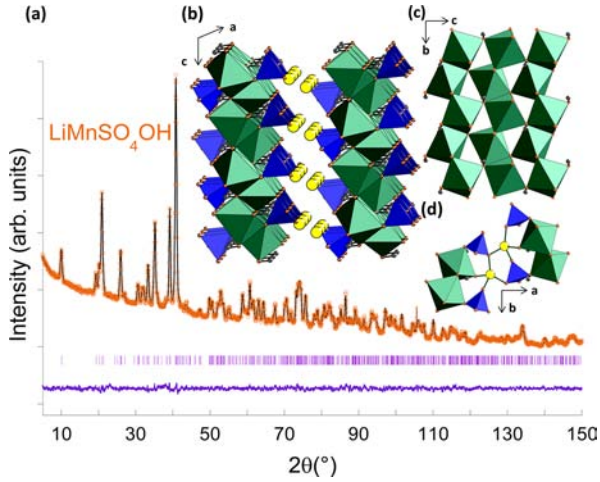

Figure 2. (a) Rietveld refinement of neutron diffraction pattern of $LiMnSO_4OH$ (λ = 1.5942 Å, R_{Bragg} = 3.15%, χ^2 = 8.49). Orange dots and black and brown traces correspond to the observed, calculated, and difference, respectively. The vertical violet tick marks correspond to the Bragg peaks. (b) Structure of $LiMSO_4OH$ viewed down the [001] direction. (c) View of a layer made of edge-sharing MO_6 octahedra forming ribbons connected through vertices. (d) Connectivity of lithium atoms between layers. M atoms are in the center of green octahedra, SO_4 is blue, O is orange, Li is yellow, and H is represented as small black spheres.

The structure of this $LiMSO_4OH$ family of compounds is displayed in Figure 2b. FeO_6 octahedra share edges to form zigzag chains running along the [010] direction. These chains are connected by vertices to form a layered structure (see Figure 2c). SO_4 tetrahedra are linked via vertices to the FeO_6 octahedra on each side of the layer. Lithium atoms are tetrahedrally coordinated by oxygen atoms and sit in the space between the layers (Figure 2d).

Figure 3a compares the XRD patterns for the Fe-, Co-, and Mn-based $LiMSO_4OH$ samples. Note the shift in 2θ to higher angles with a decrease in lattice parameters going from Mn to Co based on simple ionic radius considerations ($r(Mn^{2+})$ > $r(Fe^{2+})$> $r(Co^{2+})$). A comparison of the lattice parameters of these three isostructural compounds is provided in Figure 3b. Rietveld refinements of $LiFeSO_4OH$ and $LiCoSO_4OH$ against the XRD pattern are reported in Figures S5 and S6, and the atomic positions for $LiCoSO_4OH$ are reported in Table S2. Note that even though we observed the formation of the Ni-based intermediate $Ni_3(SO_4)_2(OH)_2$, the $LiNiSO_4OH$ phase could not be obtained. We do not currently have an explanation for why the Ni phase does not form, besides noting that the corresponding 3d-metal fluorosulfate ($LiNiSO_4F$) phase was also the most difficult to obtain pure in the $LiMSO_4F$ series. It is possible that the Ni^{2+} (d^8) configuration, which usually favors MO_6 distortion, plays a role in our inability to stabilize the $LiNiSO_4F(OH)$ phases.

dx.doi.org/10.1021/ja3125492 | J. Am. Chem. Soc. 2013, 135, 3653−3661

Table 3. Structure of $LiMnSO_4OH$ Deduced from Rietveld Refinement of High-Resolution Neutron Powder Diffraction Pattern[a]

	atomic positions for $LiMnSO_4OH$					
atom	site	x	y	z	B_{iso} (Å^2)	BVS
Mn	4*e*	0.5638(6)	0.2690(8)	0.6304(7)	1.33[b]	1.99(1)
S	4*e*	0.7923(6)	0.5637(1)	0.9878(8)	0.85(9)	5.81(5)
O1	4*e*	0.5781(3)	0.4270(6)	0.3747(4)	1.03(5)	1.79(1)
O2	4*e*	0.6498(3)	0.9329(5)	0.5259(4)	1.26(6)	2.07(3)
O3	4*e*	0.7676(4)	0.0425(5)	0.3009(4)	0.91(5)	2.04(3)
O4	4*e*	0.1478(4)	0.1883(6)	0.0072(5)	1.37(6)	1.91(3)
O5	4*e*	0.0966(4)	0.9194(6)	0.3657(5)	1.47(6)	2.00(3)
Li	4*e*	0.0674(9)	0.934(2)	0.809(1)	1.24(17)	1.01(2)
H	4*e*	0.3247(6)	0.008(1)	0.0909(9)	2.70(13)	1.00(1)

[a]The table includes bond valence sum (BVS) for each atom. Lattice parameters and space group are given in Figure 3. [b]$\beta 11 = 27(6)$, $\beta 22 = 118(19)$, $\beta 33 = 59(9)$, $\beta 12 = 24(8)$, $\beta 13 = -7(6)$, and $\beta 23 = -32(12)$ ($\times 10^4$).

Table 4. Structure of $LiFeSO_4OH$ Deduced from Rietveld Refinement of High-Resolution Neutron Powder Diffraction Pattern[a]

	atomic positions for $LiMnSO_4OH$					
atom	site	x	y	z	B_{iso}(Å^2)	BVS
Fe	4*e*	0.5551(2)	0.2635(2)	0.6261(2)	0.84[b]	1.94(6)
S	4*e*	0.7922(4)	0.5615(8)	0.9853(6)	0.75(6)	5.91(4)
O1	4*e*	0.5733(2)	0.4246(3)	0.3739(4)	0.73(4)	1.82(1)
O2	4*e*	0.6490(2)	0.9345(4)	0.5328(4)	0.83(4)	1.89(2)
O3	4*e*	0.7647(2)	0.0471(5)	0.2989(3)	0.99(4)	2.12(3)
O4	4*e*	0.1566(2)	0.1833(3)	0.0162(3)	0.79(4)	1.92(2)
O5	4*e*	0.0954(2)	0.9209(4)	0.3656(3)	0.99(4)	2.04(2)
Li	4*e*	0.0759(7)	0.924(1)	0.822(1)	1.47(12)	1.03(1)
H	4*e*	0.3322(5)	−0.0090(6)	0.0932(6)	1.74(7)	0.93(1)

[a]The table includes bond valence sum (BVS) for each atom. Lattice parameters and space group are given in Figure 3. [b]$\beta 11 = 36(1)$, $\beta 22 = 42(4)$, $\beta 33 = 30(2)$, $\beta 12 = 4(2)$, $\beta 13 = -2.7(2)$, and $\beta 23 = -4.6(3)$ ($\times 10^4$).

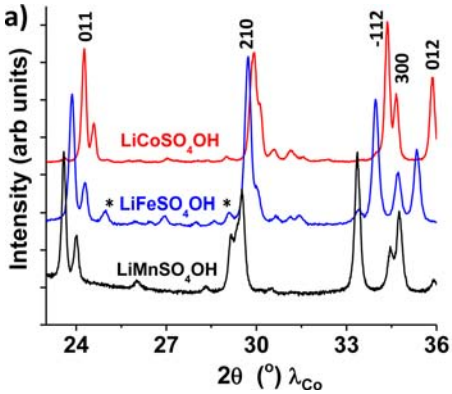

b) Comparing Lattice Parameters for $LiMSO_4OH$

	$LiCoSO_4OH$	$LiFeSO_4OH$	$LiMnSO_4OH$
Space group	$P2_1/c$	$P2_1/c$	$P2_1/c$
a(Å)	9.5842(2)	9.5147(1)	9.6156(1)
b(Å)	5.4261(2)	5.5087(1)	5.5586(1)
c(Å)	7.3240(2)	7.3755(1)	7.5465(1)
β(°)	109.699(9)	109.109(6)	109.505(1)
Volume (Å^3)	358.59(2)	365.28(1)	380.21(1)

Figure 3. (a) X-ray diffraction patterns comparing $LiMSO_4OH$ for M = Fe, Co, and Mn ($\lambda_{Co}(K\alpha_1) = 1.78897$ Å, $\lambda_{Co}(K\alpha_2) = 1.79285$ Å). The shift in 2θ to higher angles from Mn to Co, as the radius of the transition metal decreases, is clearly evident. The asterisks identify the $Li_2SO_4{\cdot}H_2O$ impurity present in the Fe phase. (b) Comparison of the unit cell parameters and volume for the three isostructural compounds.

TEM analysis of $LiFeSO_4OH$ sample prepared by mechanochemical synthesis showed highly agglomerated nanocrystals of about 10−50 nm (Figure S7). Although the material was extremely sensitive to the electron beam irradiation, we were successful in collecting ED patterns (Figure 4) by keeping the electron dose at a minimum (<5 e$^-$/Å^2). The ED patterns further confirmed the lattice parameters and, more importantly, the space group symmetry determined from PXRD.

Lastly, the thermal stability of these new phases was examined by TGA of the samples under Ar flow (Figure S8). Though the Fe phase showed lower stability (by about 100 °C) compared to Mn and Co phases, they are all stable up to temperatures of 300 °C, which is generally sufficient for materials used as insertion electrodes in Li-ion batteries. At temperatures greater than 350 °C under Ar flow, the $LiFeSO_4OH$ phase was found to decompose into a mixture of $Fe_2(SO_4)_3$, $FeSO_4$, and $Li_2Fe(SO_4)_2$ phases, with the latter being the major component.

2. Electrochemical Characterization. The electrochemical performance of $LiMSO_4OH$ samples, ball-milled (Spex, 20 min) with 25 wt% carbon black (SP), was tested vs Li in Swagelok half-cells. The electrochemical behavior was comparable for the ceramic and ball-milled samples. The voltage-composition trace for a Li/$LiFeSO_4OH$ cell (Figure 5) cycled

dx.doi.org/10.1021/ja3125492 | J. Am. Chem. Soc. 2013, 135, 3653−3661

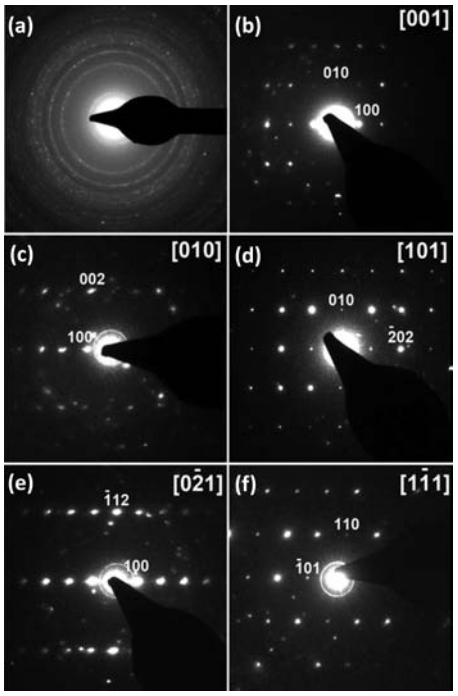

Figure 4. Electron diffraction patterns showing (a) ring and (b–f) single-crystal patterns of $LiFeSO_4OH$ prepared by ball-milling.

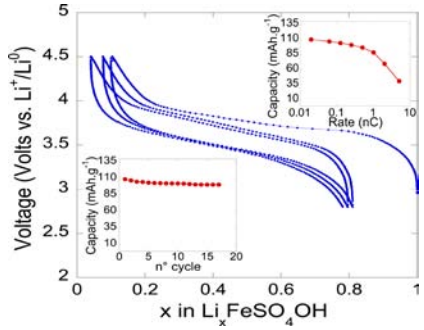

Figure 5. Cycling of $LiFeSO_4OH$ battery vs Li. Cycling was done at a C/20 rate using a 1 cm^2 disk electrode loaded with 8 mg of active material. The inset on the bottom-left corner shows the capacity retention as a function of cycle number. The power rate for a $LiFeSO_4OH$ electrode, as deduced from signature curves,[32] is shown in the top-right inset.

between 4.5 and 2.8 V at a rate of C/20 shows electrochemical activity centered around 3.6 V. During the first charge up to 4.2 V, about 0.9 Li^+ ion can be removed from the structure and about 0.70 Li^+ can be re-inserted during the following discharge. The discharge shows a smooth voltage decay as a function of composition, but the subsequent charge does not exactly trace back the first one, in terms of profile. At the initial stage of the first charge, there is an oxidation phenomenon, not yet identified, which is no longer present on the second charge. Moreover, the oxidation curve is not perfectly S-type, unlike that of discharge. This difference is clearly indicated by the derivative plot which shows a nice symmetric peak on reduction as opposed to two poorly separated peaks on oxidation (Figure 6), likely due to subtle structural changes. Nevertheless, subsequent charge/discharge curves were found to neatly superimpose, leading to a steady capacity retention of about 100–110 mAh/g upon cycling. As deduced from power rate measurements, this electrode material displays decent rate capabilities and maintains 85% of its initial capacity at a C rate (inset of Figure 5). Electrode optimization enlisting various grinding times as well as carbon loading and changing the nature of the added carbon is presently being explored to improve electrode kinetics.

Moving to Mn- and Co-based hydroxysulfates, Li/$LiMnSO_4OH$ and $LiCoSO_4OH$ half-cells were assembled and cycled at C/30 up to 5 V, and the derivative curves ($dx/dV = f(V)$) are reported in Figure 6. For the Mn-based cell, we note an oxidation peak at 4.7 V, which is due to either electrolyte oxidation or material decomposition since no reduction peak, and hence no capacity, was observed when the current polarity was changed and the cell was placed on discharge (Figure 6). This is in contrast with the Co-based cells, which show an oxidation plateau at 4.8 V and a reduction one at 4.6 V vs Li^+/Li^0, suggesting redox activity associated with Co^{3+}/Co^{2+} couple at an average voltage of 4.7 V vs Li^+/Li^0. However, the oxidation peak is larger than the reduction one (accounting for 0.2 Li^+ per formula unit), indicating poor reversibility, likely due to the limited electrolyte stability rather than an intrinsic material limitation with respect to Li insertion/de-insertion. Irrespective of the charging conditions used (cutting voltage up to 5.2 V and charging times corresponding to $\Delta x = 1$), we could never obtain discharge capacities exceeding 0.2 Li^+ per $Li_{1-x}CoSO_4OH$ per formula unit. The performance of this material is being further investigated using solid electrolytes, which are capable of sustaining high voltages.

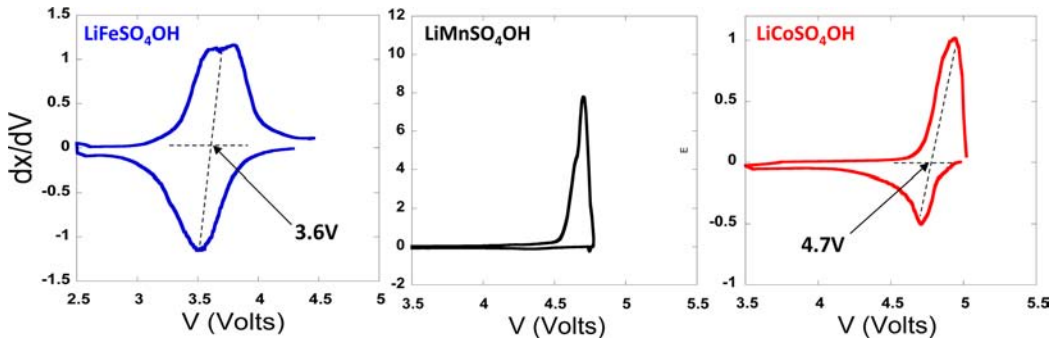

Figure 6. Comparing the derivative curves for $LiMSO_4OH$ (M = Fe, Mn, Co) cycled vs Li. The Co phase shows the highest redox (~4.7 V vs Li^+/Li^0) activity as compared to the Fe phase (~3.6 V vs Li^+/Li^0). Therefore, a limited amount of Li can be removed from the Co phase (0.2 per formula unit). Lastly, the Mn phase does not show any electrochemical activity vs Li^+/Li^0, as indicated by the absence of a redox peak on discharge. On charge, an oxidation peak corresponding to the electrolyte decomposition is observed.

dx.doi.org/10.1021/ja3125492 | J. Am. Chem. Soc. 2013, 135, 3653–3661

To obtain an understating of the Li insertion/de-insertion mechanism in these materials, *in situ* XRD measurements were conducted and XRD patterns collected on charge and subsequent discharge for every change $\Delta x = 0.1$ (Figure 7).

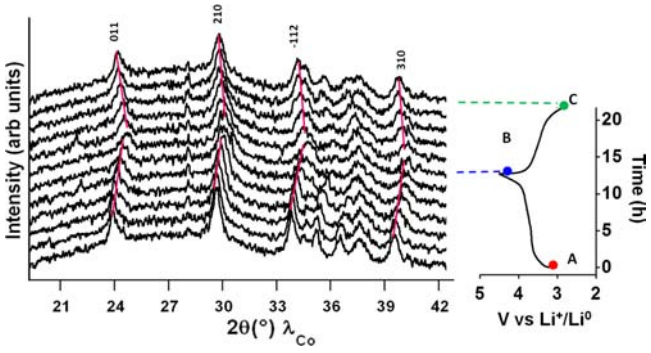

Figure 7. *In situ* XRD patterns of $LiFeSO_4OH$ battery cycling vs Li at C/20 confirms solid solution behavior (λ_{Co}). The voltage vs time plot corresponding to the *in situ* cycling is also shown on the right panel: (A) beginning of charge, (B) beginning of discharge, and (C) end of discharge.

As the Li/$LiFeSO_4OH$ cell was being charged, a gradual shift in the position of the peaks toward higher 2θ angles was observed. This shift suggests a decrease in unit cell volume, which is in accordance with the shift from Fe^{2+} to a smaller Fe^{3+} cation. Our results show that the Li insertion/de-insertion process enlists a solid solution mechanism rather than a biphasic domain, which is in agreement with the slope presented by the voltage−composition curves. The reverse peak shift observed on the subsequent discharge indicates full reversibility of the process based on the similarity between the pristine electrode (point A) and the charged/discharged electrode (point C). Therefore, no specific structural features corresponding to the slight split in the oxidation peak seen in the derivative curve (Figure 6) were identified. Elucidating this observed voltage anomaly during the first charge cycle requires *in situ* synchrotron measurements. Rietveld refinement for the X-ray pattern of electrochemically delithiated sample (charged to 4.5 V at C/30 rate and washed with DMC and dried: $Li_{0.1}FeSO_4OH$) was conducted to obtain structural information. Despite the low crystalline quality of the powder and the presence of carbon, the X-ray pattern was fully indexed with a monoclinic unit cell (space group $P2_1/c$) of $a = 9.481(3)$ Å, $b = 5.296(2)$ Å, $c = 7.207(2)$ Å, $\beta = 110.55(3)°$, and $V = 338.9(2)$ Å^3. These results suggest a volume contraction ($\Delta V/V$) of about 7%, which is comparable to that observed in $LiFePO_4$[28] and hence a positive attribute for battery applications.

DISCUSSION

Using both mechanochemical synthesis and low-temperature solid-state reactions, we unveiled a new class of Li-based hydroxysulfates materials, among which $LiFeSO_4OH$ upon optimization could be an attractive positive electrode material for Li-ion batteries. These new phases provide interesting structural and chemical aspects worth discussing with respect to their phosphate, fluorosulfate, and other polyanionic analogues.

Similar to $LiFeSO_4F$, $LiFeSO_4OH$ shows polymorphism and can adopt either the *tavorite* structure or the layered one described here. The layered polymorph shows a redox potential of 3.6 V compared to 3.2 V for *tavorite* $LiFeSO_4OH$. This observed difference in redox potentials cannot be explained using Goodenough's inductive effect,[6] since both polymorphs share the same anionic groups (SO_4^{2-} and OH^-). Hence, we must return to the ionic−covalent character of the metal−anion bonding which is determined from an amalgam of several structural features among coordination environment, sites energies, crystal fields, crystal density, and others. For example, the Fe−O bond distance was successfully used to account for the different Fe^{3+}/Fe^{2+} redox potentials in the α, β, and γ Li_2FeSiO_4 polymorphs.[29] The bond distances, though to a lesser degree, were also used to explain differences between the *tavorite*/*triplite*/*sillimanite* $LiFeSO_4F$ polymorphs.[14] However, applying the same concept is not fully conclusive in the $LiFeSO_4OH$ case. The $FeO_4(OH)_2$ octahedron in layered $LiFeSO_4OH$ is highly distorted (Fe−O distances ranging from 2.05 to 2.24 Å), while there are two Fe sites in $LiFeSO_4OH$ *tavorite* with Fe−O distances of 2.16 and 2.14 Å; therefore, a simple bond averaging leads to similar Fe−O distances (2.153 and 2.149 Å) for the two polymorphs. Hence, there is a need to identify another parameter, which accounts for the observed voltage difference between the two $LiFeSO_4OH$ structures.

Besides the bond lengths, another parameter used to explain these voltage trends is the density of the compounds; densely packed compounds have bonds with a higher ionic character and therefore demonstrate higher redox potentials. Such a trend was validated by the polymorphism in $LiFeSO_4F$, since the denser polymorph (*triplite*) showed the higher potential.[13] The same trend is observed here as well, with the layered $LiFeSO_4OH$ polymorph which is denser (3.20 g/cm^3) than its *tavorite* form (3.10 g/cm^3) showing the higher potential of the two (3.6 vs 3.2 V).[10,16] This difference in density can be explained from structural considerations as well, since the number of Fe−Fe interactions is quite large for the layered structure in which the $FeO_4(OH)_2$ octahedra are both edge- and corner-sharing as opposed to solely corner-sharing in the case of *tavorite*. However, reaching higher voltages by just increasing crystal density is not feasible for practical applications, as it limits ion diffusion and therefore results in poor rate capabilities. Our layered $LiFeSO_4OH$ electrodes show poor kinetics, but whether it is related to their crystal density or purely coincidental is not obvious. We hope our observations provide an impetus for theorists to develop a reliable method for predicting redox potentials and ion diffusion observed in these polymorphs.

A general trend observed both experimentally and theoretically in any family of polyanionic compounds (phosphates, silicates, etc.) is an increase in the potential of the $M^{(n+1)+} \rightarrow M^{n+}$ redox couple moving from Fe to Mn, to Co, and to Ni. $LiCoSO_4OH$ obeys this trend since its potential of 4.7 V is higher than 3.6 V vs Li^+/Li^0 of $LiFeSO_4OH$. In this context, the inactivity of $LiMnSO_4OH$ comes as a surprise, as it is isostructural to the Fe and Co phases. However, we also previously observed a similar trend in the fluorosulfate family, where *triplite* $LiMnSO_4F$ was electrochemically inactive with respect to Li, while *triplite* $LiFeSO_4F$ was found to reversibly react at 3.9 V vs Li^+/Li^0. Turning to the Mn-based phosphates, borates, and silicates, while they are electrochemically active toward Li, they generally display sluggish kinetics. The results presented here further highlight the complexity of the Mn-based compounds and our poor understanding of their structure and properties. Also, DFT calculations have encountered difficulties in simulating these compounds, suggesting a need for new methods to reliably predict the structure and electrochemical properties of these phases.

dx.doi.org/10.1021/ja3125492 | J. Am. Chem. Soc. 2013, 135, 3653−3661

Whether this observed anomaly in Mn phases is related to the Jahn−Teller effect of Mn^{3+} is not clear, but is a question worth consideration.

The feasibility of ball-milling to prepare sulfates, while the technique has failed in making oxides and phosphates, is worth discussing. We believe this is due to both the low thermal stability (<400 °C) of the sulfate precursors (MSO_4) and the heat generated by the plastic deformation of particles during ball-milling. Indeed, highly energetic ball-milling can achieve local temperatures up to a few hundred degrees.[30,31] Also, it is well known that ball-milling generates defects and disorders which allow for the stabilization of amorphous and metastable phases under ambient conditions. In fact, of the $LiMSO_4OH$ materials reported here, only the Fe phase, which has higher metastability (lower decomposition temperature, Figure S8) compared to the Mn and Co phases, could be prepared via ball-milling. For the same reasons, crystalline phosphates are also difficult to prepare by ball-milling.

CONCLUSIONS

A new family of polyanionic hydroxysulfates $LiMSO_4OH$ with M = Fe, Co, and Mn was successfully synthesized, and the electrochemical activity of these compounds was tested. Synthesis by ball-milling occurs through an intermediate $M_3(SO_4)_2(OH)_2$ phase, the structure of which is related to the mineral *caminite*. Further, the desired $LiMSO_4OH$ phase presents a layered structure, as revealed by X-ray and neutron powder diffraction experiments. $LiFeSO_4OH$ was prepared by both ceramic and mechanochemical methods and showed the best electrochemical activity of the three isostructural $LiMSO_4OH$ materials studied (M = Fe, Co, Mn). Besides unveiling a new class of attractive electrode materials, we also further demonstrate the potential of mechanochemical synthesis in stabilizing new low-temperature metastable phases, an approach which can be used to explore other families of polyanionic compounds.

ASSOCIATED CONTENT

Supporting Information

Tables listing synthesis conditions for sulfate precursors and atomic positions of $LiCoSO_4OH$; Rietveld refinements of $LiFeSO_4OH$ NPD pattern and refinements of XRD of $LiFeSO_4OH$, $LiCoSO_4OH$, and $Mn_3(SO_4)_2(OH)_2$; TEM images of $LiFeSO_4OH$ and TGA of $LiMSO_4OH$; X-ray patterns of $LiFeSO_4OH$ as a function of ball-mill time; representative Mössbauer spectra for $LiFeSO_4OH$; CIF files of $LiMSO_4OH$ and $M_3(SO_4)_2(OH)_2$ structures. This material is available free of charge via the Internet at http://pubs.acs.org.

AUTHOR INFORMATION

Corresponding Author

jean-marie.tarascon@u-picardie.fr

Notes

The authors declare no competing financial interest.

ACKNOWLEDGMENTS

The authors acknowledge Matthieu Courty for TGA measurements, Moulay Tahar Sougrati for Mössbauer spectroscopy, and Jean-Noël Chotard for fruitful discussions and help in measuring powder diffraction patterns. We also thank Thomas Hansen for help during neutron diffraction experiments and Institut Laue Langevin for awarding neutron beamtime. This work was funded by the "Réseau sur le Stockage Electrochimique de l'Energie (RS2E)". G.V.T. acknowledges support from the ERC grant "Countatoms" and the 7th framework EC project "ESMI".

REFERENCES

(1) Thackeray, M. M.; Johnson, C. S.; Vaughey, J. T.; Li, N.; Hackney, S. A. *J. Mater. Chem.* **2005**, *15*, 2257.
(2) Padhi, A. K.; Nanjundaswamy, K. S.; Goodenough, J. B. *J. Electrochem. Soc.* **1997**, *144*, 1188.
(3) Nyten, A.; Abouimrane, A.; Armand, M.; Gustafsson, T.; Thomas, J. O. *Electrochem. Commun.* **2005**, *7*, 156.
(4) Nishimura, S.; Nakamura, M.; Natsui, R.; Yamada, A. *J. Am. Chem. Soc.* **2010**, *132*, 13596.
(5) Yamada, A.; Iwane, N.; Harada, Y.; Nishimura, S.; Koyama, Y.; Tanaka, I. *Adv. Mater.* **2010**, *22*, 3583.
(6) Padhi, A. K.; Manivannan, V.; Goodenough, J. B. *J. Electrochem. Soc.* **1998**, *145*, 1518.
(7) Recham, N.; Chotard, J. N.; Dupont, L.; Delacourt, C.; Walker, W.; Armand, M.; Tarascon, J. M. *Nat. Mater.* **2010**, *9*, 68.
(8) Recham, N.; Rousse, G.; Sougrati, M. T.; Chotard, J. N.; Frayret, C.; Sathiya, M.; Melot, B. C.; Jumas, J. C.; Tarascon, J. M. *Chem. Mater.* **2012**, *24*, 4363.
(9) Melot, B. C.; Rousse, G.; Chotard, J. N.; Kemei, M. C.; Rodriguez-Carvajal, J.; Tarascon, J. M. *Phys. Rev. B* **2012**, *85*, 4415.
(10) Ati, M.; Sougrati, M. T.; Rousse, G.; Recham, N.; Doublet, M. L.; Jumas, J. C.; Tarascon, J. M. *Chem. Mater.* **2012**, *24*, 1472.
(11) Ati, M.; Sathiya, M.; Boulineau, S.; Reynaud, M.; Abakumov, A.; Rousse, G.; Melot, B.; Van Tendeloo, G.; Tarascon, J.-M. *J. Am. Chem. Soc.* **2012**, *134*, 18380.
(12) Melot, B. C.; Rousse, G.; Chotard, J. N.; Ati, M.; Rodriguez-Carvajal, J.; Kemei, M. C.; Tarascon, J. M. *Chem. Mater.* **2011**, *23*, 2922.
(13) Barpanda, P.; Ati, M.; Melot, B. C.; Rousse, G.; Chotard, J. N.; Doublet, M. L.; Sougrati, M. T.; Corr, S. A.; Jumas, J. C.; Tarascon, J. M. *Nat. Mater.* **2011**, *10*, 772.
(14) Ati, M.; Melot, B. C.; Rousse, G.; Chotard, J.-N.; Barpanda, P.; Tarascon, J.-M. *Angew. Chem., Int. Ed.* **2011**, *50*, 10574.
(15) Ati, M.; Melot, B. C.; Chotard, J. N.; Rousse, G.; Reynaud, M.; Tarascon, J. M. *Electrochem. Commun.* **2011**, *13*, 1280.
(16) Reddy, M. A.; Pralong, V.; Caignaert, V.; Varadaraju, U. V.; Raveau, B. *Electrochem. Commun.* **2009**, *11*, 1807.
(17) Rietveld, H. M. *J. Appl. Crystallogr.* **1969**, *2*, 65.
(18) Rodríguez-Carvajal, J. *Phys. B: Condensed Matter* **1993**, *192*, 55.
(19) Disma, F.; Aymard, L.; Dupont, L.; Tarascon, J. M. *J. Electrochem. Soc.* **1996**, *143*, 3959.
(20) SalverDisma, F.; Lenain, C.; Beaudoin, B.; Aymard, L.; Tarascon, J. M. *Solid State Ionics* **1997**, *98*, 145.
(21) Haymon, R. M.; Kastner, M. *Am. Mineral.* **1986**, *71*, 819.
(22) Fleet, M. E.; Knipe, S. W. *Acta Crystallogr., Sect. B-Struct. Commun.* **1997**, *53*, 358.
(23) Shannon, R. D. *Acta Crystallogr., Sect. A* **1976**, *32*, 751.
(24) Brown, I. D.; Altermatt, D. *Acta Crystallogr., Sect. B* **1985**, *41*, 244.
(25) Reynaud, M.; Barpanda, P.; Rousse, G.; Chotard, J. N.; Melot, B. C.; Recham, N.; Tarascon, J. M. *Solid State Sci.* **2012**, *14*, 15.
(26) Boultif, A.; Louer, D. *J. Appl. Crystallogr.* **1991**, *24*, 987.
(27) Altomare, A.; Burla, M. C.; Camalli, M.; Carrozzini, B.; Cascarano, G. L.; Giacovazzo, C.; Guagliardi, A.; Moliterni, A. G. G.; Polidori, G.; Rizzi, R. *J. Appl. Crystallogr.* **1999**, *32*, 339.
(28) Rousse, G.; Rodriguez-Carvajal, J.; Patoux, S.; Masquelier, C. *Chem. Mater.* **2003**, *15*, 4082.
(29) Sirisopanaporn, C.; Masquelier, C.; Bruce, P. G.; Armstrong, A. R.; Dominko, R. *J. Am. Chem. Soc.* **2011**, *133*, 1263.
(30) Maurice, D. R.; Courtney, T. H. *Metallurg. Trans. a-Phys. Metallurgy Mater. Sci.* **1990**, *21*, 289.
(31) Eckert, J.; Schultz, L.; Urban, K. *J. Less-Common Met.* **1988**, *145*, 283.

(32) Doyle, M.; Newman, J.; Reimers, J. *J. Power Sources* **1994**, *52*, 211.